ACS Catalysis

pubs.acs.org/acscatalysis Research Article

Insights into the Pyridine-Modified MOR Zeolite Catalysts for DME Carbonylation

Kaipeng Cao,[§] Dong Fan,[§] Lingyun Li, Benhan Fan, Linying Wang, Dali Zhu, Quanyi Wang, Peng Tian,* and Zhongmin Liu*

Cite This: *ACS Catal.* 2020, 10, 3372−3380 Read Online

ACCESS | Metrics & More | Article Recommendations | Supporting Information

ABSTRACT: Pyridine-modified mordenite (MOR) zeolite catalysts have attracted great attention in recent years due to their unique shape selectivity within eight-membered ring (8-MR) side pockets for dimethyl ether (DME) carbonylation to methyl acetate (MA) and syngas conversion to ethylene. Herein, aimed at elucidating pyridine modification−carbonylation activity relationships and developing high-performance catalysts, we investigated the adsorption/desorption behaviors of pyridine on MOR zeolites with varying Si/Al ratios and their impact on DME carbonylation. Instead of the previously proposed selective adsorption of pyridine in 12-MR channels, pyridine is revealed to penetrate into 8-MR side pockets of MOR zeolites and interact with acidic hydroxyls therein. Upon heating, pyridine in pockets desorbs preferentially, likely arising from the lower stability of pyridine adspecies in constrained spaces. This well explains the observed increment of carbonylation activity following the increase of pretreatment temperature. Unprecedentedly, high MA yield (7.2 mmol/(h g)) has been achieved on pyridine-modified MOR (Si/Al = 13.8) under controlled pyridine desorption conditions, resulting from the joint contributions of better diffusion properties and larger amounts of active acid sites. Moreover, the catalytic activity of Brønsted acid sites within 8-MR pockets is demonstrated to be inhomogeneous, closely associated with their locations.

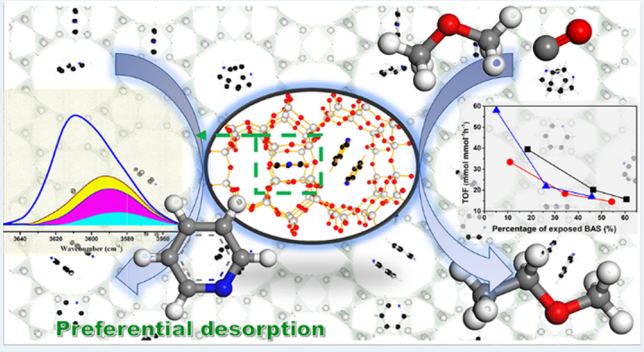

KEYWORDS: *MOR, DME carbonylation, FTIR, zeolite, pyridine adsorption*

INTRODUCTION

Since the first report of selective carbonylation of dimethyl ether (DME) over zeolite catalysts by Iglesia and his colleagues in 2006, this reaction has been attracting great attention in the field of heterogeneous catalysis[1−3] because it offers an effective way to enhance the value of C1 chemicals via the formation of C−C bonds. Methyl acetate (MA), the highly selective product of DME carbonylation, could be further hydrogenated to produce ethanol, which acts as an important chemical and additive for transport fuel.[4] Thus, DME carbonylation indeed opens a novel route for ethanol production from sources such as coal and natural gas. In 2017, a commercial DME-to-ethanol (DMTE) process with a production capacity of 100 000 tons of ethanol/year, developed by the Dalian Institute of Chemical Physics (DICP), has been successfully put into operation in Shaanxi, China.[5]

Mordenite (MOR) and ferrierite (FER) zeolites have been demonstrated to be the most efficient catalysts for DME carbonylation.[6−10] In particular, MOR exhibits the highest carbonylation activity and selectivity to the desired product MA. An MOR framework consists of a parallel 12-membered ring (12-MR, 6.5 × 7.0 Å^2) and 8-MR channels (2.6 × 5.7 Å^2) along the *c* axis direction, both of which are interconnected by 8-MR side pockets (3.4 × 4.8 Å^2) along the *b* axis direction.[11,12] As the 8-MR channels along the *c* axis are too narrow for most molecules to penetrate, MOR practically behaves as a unidimensional zeolite in catalytic reactions. Previous studies have evidenced that the mechanism of DME carbonylation of acidic zeolites involves the adsorption of DME on Brønsted acid sites (BAS) to form methoxy species and their subsequent reaction with CO to yield acetyl intermediates that further react with DME to deliver MA; the rate-determining step in the carbonylation of MOR zeolite is the formation of acetyl intermediates, which preferentially occurs in the 8-MR side pockets with spatial confinement.[14−16] Several research groups have reported that DME carbonylation rates are proportional to the number of BAS in the 8-MR side pockets.[17−19] In addition, Corma et al. investigated the carbonylation activities of BAS at different crystallographic positions by quantum-chemical methods.[15] They concluded

Received: November 11, 2019
Revised: January 14, 2020
Published: February 11, 2020

that the T3-O33 position inside 8-MR pockets is the only one selective for carbonylation; both the space-confinement effect of the 8-MR pockets and the unusual orientation of the methoxy groups at T3-O33 positions contribute to the unique carbonylation behavior. The acid sites in the 12-MR main channels, on the other hand, are prone to side reactions (DME to hydrocarbons), resulting in rapid carbon deposition and quick deactivation of the MOR catalysts.[15,20] Very recently, based on Monte Carlo and molecular dynamics simulation, Zheng et al. also visited the different roles of the 8-MR and 12-MR channels in MOR zeolites, concluding that the CO aggregation properties inside the 8-MR side pockets also contributed to the unique catalytic performance of the 8-MR channels.[21]

To improve the catalytic stability of MOR zeolites in the DME carbonylation, several strategies have been developed via selectively removing/poisoning the acid sites inside the 12-MR channels, including high-temperature steam treatment (dealumination),[22] acid/alkaline treatment (dealumination),[23,24] pyridine modification,[25] etc. Among them, the pyridine modification strategy represents the most effective one, as the catalytic lifespan of pyridine pre-adsorbed MOR zeolites is evidently superior to those prepared by other methods. Very recently, pyridine-modified MOR zeolite was also reported to be a highly selective catalyst for syngas conversion to ethylene and methanol to olefin reaction,[26,27] verifying again the effectiveness of such a strategy and the peculiarity of the 8-MR side pockets with spatial confinement.

Based on carefully prepared H-MOR zeolite (Si/Al ≈ 10) without dealumination, Maache et al. first reported that the BAS inside the 12-MR channels can be selectively titrated by pyridine, whereas the acid sites located in the 8-MR pockets are inaccessible due to the large molecular diameter of pyridine.[45] However, it is very difficult to avoid the occurrence of dealumination during the practical preparation (such as calcination or pretreatment process) of MOR zeolites,[28−32] which would create silanol or aluminol defects inside the zeolite framework. This is also the case for other zeolites with lower Si/Al ratios.[30,33,34] The generation of defect sites in MOR zeolite may change the diffusion properties of reactants/products and the accessibility of BAS in 8-MR side pockets. It is thus important to learn the adsorption/desorption behaviors of pyridine molecules on the de facto imperfect MOR zeolite and their influence on the catalytic property, which would prompt the improvement of pyridine-modified MOR catalysts.

In this contribution, the sorption behaviors of pyridine on MOR zeolites with varying Si/Al ratios (Si/Al = 7−20) were monitored by Fourier transform infrared (FTIR) and their impact on DME carbonylation was explored. Spectroscopic results evidenced that pyridine could actually interact with the hydroxyl protons in the 8-MR side pockets of these MOR catalysts. However, pyridine desorbs preferentially from the pockets when heated, which accounts for the good stability and high carbonylation activity of the pyridine-modified catalysts. The effect of Si/Al ratios on pyridine modification and DME carbonylation activity and the inhomogeneity of the active centers inside the 8-MR side pockets were also studied.

EXPERIMENTAL SECTION

Catalyst Preparation. MOR zeolites were prepared through a hydrothermal synthesis method. Sodium hydroxide, sodium aluminate, tetraethylammonium hydroxide solution (TEAOH, 35 wt %), and H_2O were first mixed at room temperature and stirred until they are completely dissolved. Subsequently, under intense stirring, silica sol was added dropwise into the above solution. After aging at ambient temperature for 1 h, seed crystals (2 wt % relative to SiO_2) were added and the mixture underwent further agitation for another 1 h. The molar compositions of the obtained reaction gels are listed in Table S1. The mixture was further transferred into a 100 mL autoclave and crystallized at 170 °C for 48 h under static conditions. After crystallization, the solid products were washed with distilled water, recovered by centrifugation and dried at 120 °C for 12 h. To remove the organic amines, the sample was heated (1 °C/min) to 550 °C under dry air and kept at this temperature for 4 h. The resultant sample was further transformed into its proton type by ammonium exchange within 1 mol/L NH_4NO_3 solution (1 h@80 °C, repeated three times) and calcination at 550 °C (temperature ramp rate: 1 °C/min) for 4 h under dry air.

Catalyst Characterization. The powder X-ray diffraction (XRD) patterns of the as-synthesized samples were recorded using a PANalytical X'Pert PRO X-ray diffractometer with Cu Kα radiation (λ = 0.154059 Å) at 40 kV and 40 mA from 5 to 50°. The elemental compositions of the as-synthesized samples were determined on a Philips Magix-601 X-ray fluorescence (XRF) spectrometer. The scanning electron microscopy (SEM) images of the synthesized samples were recorded on a Hitachi SU8020 SEM equipment. N_2 adsorption and desorption analysis was carried out on a Micromeritics ASAP 2020 analyzer. The total surface area was calculated based on the Brunauer−Emmett−Teller (BET) method. The micropore volume and area were derived by the *t*-plot method. Temperature-programmed desorption of ammonia (NH_3-TPD) analysis was performed using 100 mg powder of H-MOR zeolites at the temperature range of 100−700 °C after sample pretreatment at 450 °C for 1 h under He flow using Micromeritics AutoChem II 2920 equipped with a thermal conductivity detector (TCD). Solid-state NMR spectra were recorded on a Bruker Avance III 600 MHz spectrometer. Before ^{1}H magic-angle spinning (MAS) NMR measurements, the samples were dehydrated at 420 °C under a vacuum below 10^{-3} Pa for 20 h. ^{1}H MAS NMR spectra were collected at 600.13 MHz with a 3.2 mm HXY probe using a Hahn-Echo pulse sequence with a $\pi/2$ pulse of 3.2 μs, a recycle delay of 10 s, and a spinning speed of 20 kHz. The chemical shifts were referenced to adamantane at 1.74 ppm.

Fourier transform infrared spectra of pyridine (Py-FTIR) analysis were recorded on Bruker Tensor 27 instrument with an mercury cadmium telluride (MCT) detector. The samples (20 mg) were pressed into a self-supporting wafer and placed into a quartz cell. Subsequently, the samples were pretreated at 400 °C for 30 min under vacuum. After pretreatment, the samples were cooled down to room temperature. The spectra of MOR samples without pyridine perturbation were subsequently recorded from 4000 to 1000 cm^{-1}. Afterward, pyridine was introduced into the cell until complete saturation, followed by evacuation of the IR cell for 30 min to remove physisorbed pyridine. The desorption process of pyridine was monitored by heating the sample up to desired temperatures with a heating rate of 5 °C/min under vacuum. Each spectrum was obtained by averaging 64 scans with a resolution of 4 cm^{-1}, and all of the spectra are recorded at room temperature. Note that the heating rate of the treatment processes was initially set at 1 °C/min to avoid the dealumination of the samples. However, the resultant spectra show no obvious

https://dx.doi.org/10.1021/acscatal.9b04890
ACS Catal. 2020, 10, 3372−3380

difference with those obtained at 5 °C/min, and the experiments are consequently conducted with a heating rate of 5 °C/min (Figure S1).

Catalytic Testing. DME carbonylation reactions were performed in a fixed-bed reactor, and 0.5 g of the catalyst (40−60 mesh) was loaded into the reactor and pretreated (heating rate 1 °C/min) in Ar at 400 °C for 2 h. Afterward, the sample was purged with a pyridine−Ar mixture (30 mL/min) for 20 min at 200 °C and subsequently flushed with Ar at certain temperatures (200, 300, 400, 500 °C), until no obvious pyridine can be detected by a gas chromatograph. Finally, the temperature was reduced to 200 °C and a reactant gas mixture ($DME/CO/N_2$ = 5:35:60) was introduced with a gas hourly space velocity (GHSV) of 3600 mL/(g h). The reaction pressure was 2.0 MPa. The products were analyzed online by a gas chromatograph (Agilent 7890B) equipped with a TCD and an flame ionization detector (FID) using a TDX-1 packed column and a PoraPLOT Q capillary column, respectively.

RESULTS AND DISCUSSION

Structural and Compositional Analysis. Five MOR zeolites with Si/Al ratios between 7 and 20 were synthesized. The elemental compositions of the as-synthesized samples, derived from XRF analysis, are listed in Table 1. To clarify, the samples are denoted MOR(7.0), MOR(9.7), MOR(13.8), MOR(16.5), and MOR(19.4), with the values in the parentheses indicating their Si/Al ratios. The XRD patterns of the as-synthesized samples are presented in Figure S2, all of which could be well-indexed to the MOR structure, indicating their good purity. SEM images (Figure S3) reveal that the MOR samples with lower Si/Al ratios have aggregated morphologies of nanograins, which is likely owing to the use of seeds for the synthesis. With the increase of Si/Al ratios (samples MOR(13.8), MOR(16.5) and MOR(19.4)), the primary particles become more closely packed and even merge into bulk particles. The change in morphology following the increase of Si/Al ratios is consistent with increased crystallinity as evidenced by the XRD results. The N_2 physisorption isotherms of the samples are displayed in Figure S4, which can be regarded as type I or composite of type I plus type IV isotherms. For samples MOR(7.0) and MOR(9.7), very small hysteresis loops of H4-type are observed, likely resulting from the stacking voids of nanograins. The corresponding textural properties are listed in Table 1. The micropore surface areas and micropore volumes of the samples are in the range of 371−394 m^2/g and 0.18−0.19 cm^3/g, respectively, verifying their good crystallinity.

Table 1. Elemental Compositions and Textural Properties of the Samples

		surface area[b] (m^2/g)			pore volume[c] (cm^3/g)		
sample	Si/Al ratio[a]	S_{BET}	S_{micro}	S_{ext}	V_{total}	V_{micro}	V_{meso}
MOR(7.0)	7.0	438	371	67	0.25	0.18	0.07
MOR(9.7)	9.7	461	394	67	0.26	0.19	0.07
MOR(13.8)	13.8	459	390	69	0.25	0.19	0.06
MOR(16.5)	16.5	438	384	54	0.24	0.19	0.06
MOR(19.4)	19.4	447	394	53	0.24	0.19	0.05

[a]Derived from XRF analysis. [b]S_{BET}: BET surface area, S_{micro}: *t*-plot micropore surface area, $S_{ext} = S_{BET} - S_{micro}$. [c]$V_{total}$: total volume absorbed at P/P_0 = 0.99, V_{micro}: *t*-plot micropore volume, $V_{meso} = V_{total} - V_{micro}$.

Acid Properties. NH_3-TPD was employed to probe the acid properties of the samples, and the corresponding profiles are presented in Figure S5. The existence of two obvious NH_3 desorption peaks could be observed for all of the investigated samples. The low-temperature desorption peaks centered at around 195 °C are due to NH_3 desorption from weak acid sites and physiosorbed NH_3, while the peaks centered at relatively high temperatures are attributed to NH_3 desorption from strong acid sites.[24,35−39] The NH_3 desorption temperatures associated with strong acid sites rise in parallel with the increase of the Si/Al ratio until 13.8, indicating a gradual increase of acid strength. The reason could be attributed to the decreased number of Al atoms occupying the next-nearest-neighbor (NNN) sites in the MOR framework.[30,40] With a further increase of the Si/Al ratio to 16.5 and 19.4, the high-temperature desorption peak moves toward a lower temperature (from 530 to 500 °C). Given that the chance of Al atoms at the NNN sites is low in the samples with high Si content, this shift should not be interpreted as the decrease of acid strength. Likely, the reduced acid density on the high-Si samples lightens the probability of re-adsorption of desorbed NH_3 and thus leads to a low-temperature shift.[41−43] The deconvoluted results of the NH_3-TPD profiles are presented in Figure S5 and Table 2. Herein, NH_3 desorption at a higher temperature range is deconvoluted into two peaks, representing the moderate and strong acid sites, respectively. The total acid amounts of the samples show a decreasing trend with the increase of the Si/Al ratios.

Figure 1 illustrates the FTIR spectra of the hydroxyl vibration region of the H-MOR samples. The absorption at around 3740 cm^{-1} is due to the terminal silanol groups on the external surface of the samples.[45] The signal at 3660 cm^{-1} is ascribed to the aluminol of extra-framework (EFAl) species,[46,47] which is more prominent on the samples with

Table 2. Acid Properties of the H-MOR Samples Derived from NH_3-TPD and FTIR of Pyridine Adsorption

	NH_3-TPD (mmol/g)				Py-FTIR[a] (mmol/g)		
samples	weak	moderate	strong	M + S[b]	BAS[c]	LAS[c]	BAS/LAS
MOR(7.0)	0.83	0.32	0.67	0.98			
MOR(9.7)	0.60	0.22	0.66	0.88			
MOR(13.8)	0.51	0.18	0.68	0.86	0.76	0.10	7.60
MOR(16.5)	0.44	0.15	0.59	0.75	0.66	0.09	7.33
MOR(19.4)	0.38	0.12	0.52	0.64	0.57	0.07	8.14

[a]Py-FTIR was used to evaluate the ratio of Brønsted to Lewis acid sites based on the integrated areas of absorption bands at 1540 and 1450 cm^{-1}.[44] [b]M + S = moderate + strong. All of the acid sites of the three high-Si MOR samples can be reached by pyridine (Figure 2). [c]The amounts of BAS and LAS were derived from the ratio of BAS/LAS and the (M + S) acid amount of NH_3-TPD.

https://dx.doi.org/10.1021/acscatal.9b04890
ACS Catal. 2020, 10, 3372−3380

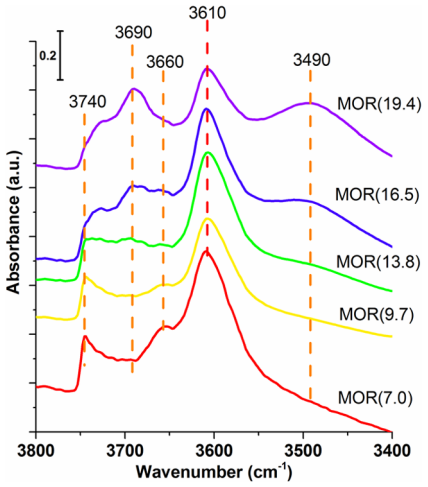

Figure 1. FTIR spectra in the ν(OH) vibration region of the H-MOR samples.

low Si/Al ratios (<10). When the Si/Al ratio increases to 13.8 or even higher, the band at 3660 cm^{-1} could hardly be discerned, indicating that the low-Si samples are more prone to dealumination. Simultaneously, two new bands at 3690 and 3490 cm^{-1} emerge in the spectrum of sample MOR(13.8), and their intensities rise with a further increment of the Si/Al ratio. The broad band at around 3490 cm^{-1} could be unambiguously ascribed to the H-bonded silanol groups inside the silanol nests.[48,49] However, the assignment of the band at 3690 cm^{-1} is not straightforward. There are two possible origins, i.e., the silanol groups inside silanol nests with trivial hydrogen bond perturbation[50] or hydroxyl pairs featuring less hydrogen bonding.[49] Considering the synchronous increase of the two bands in intensity with the Si/Al ratios, it is assumed that they are both closely related to the silanol nests. The appearance of silanol and aluminol on the samples is also confirmed by ^{1}H MAS NMR spectra (Figure S6). The deconvoluted results confirm that the relative percentage of Al−OH decreases following the increase of sample Si/Al ratios, yet that of Si−OH gives an opposite trend.

The most prominent hydroxyl band shown in Figure 1 is located at 3610 cm^{-1}, corresponding to Brønsted hydroxyl groups, which is actually a composite band comprised of high-frequency (HF) and low-frequency (LF) components.[17,19,51,52] It has been demonstrated that the HF band (around 3612 cm^{-1}) and LF band (around 3590 cm^{-1}) are associated with bridging hydroxyls in the 12-MR and 8-MR channels, respectively, which show distinct performances in the DME carbonylation reaction.[17] Deconvolution analysis of the Brønsted hydroxyls was thus carried out to determine the acid-site distribution[17,19] (Figure S7). To eliminate the interference of the silanol and aluminol groups in deconvolution, herein, NH_3 was employed to selectively titrate the Brønsted hydroxyls at 150 °C. As the bands due to the silanol and aluminol groups were barely perturbed by NH_3, isolated bands corresponding to the bridging hydroxyls could be derived by subtracting the NH_3-titrated spectra from the original ones and used for the deconvolution analysis (Figure S8). Based on the assumption that the two hydroxyl groups possess a similar molar extinction coefficient, it is calculated that around 50% of the total BAS locates inside 8-MR side pockets, independent of the Si/Al ratios of the samples (Figure S7).

Pyridine Adsorption. Figure 2 presents the hydroxyl vibration region of the FTIR spectra of the samples before and after pyridine adsorption. Pyridine, as one of the most common probe molecules to assess the acidity of zeolite catalysts, has been reported to be effective to distinguish the acid-site distribution of MOR zeolite, via selective titration of the acid sites inside the 12-MR channels.[7,23,24,45,53] However, for samples MOR(13.8), MOR(16.5), and MOR(19.4), the bands associated with the Brønsted hydroxyls are completely eroded upon pyridine adsorption at room temperature. It implies that pyridine molecules could actually penetrate into the 8-MR side pockets and capture the protons therein. Such a contradiction with the previous findings might result from the

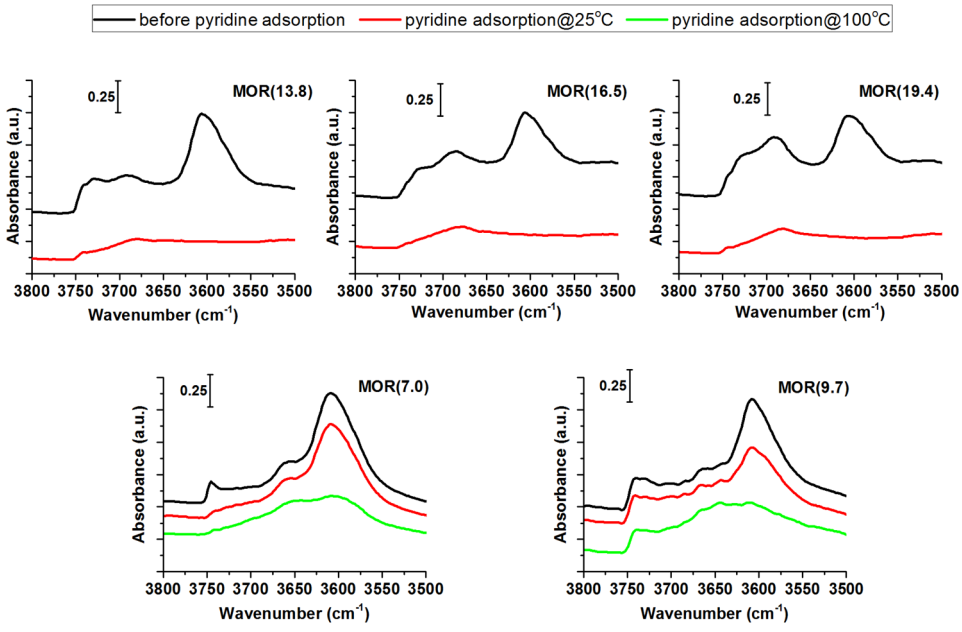

Figure 2. FTIR spectra of the ν(OH) vibration region of the H-MOR samples before and after pyridine adsorption at different temperatures.

https://dx.doi.org/10.1021/acscatal.9b04890
ACS Catal. 2020, 10, 3372−3380

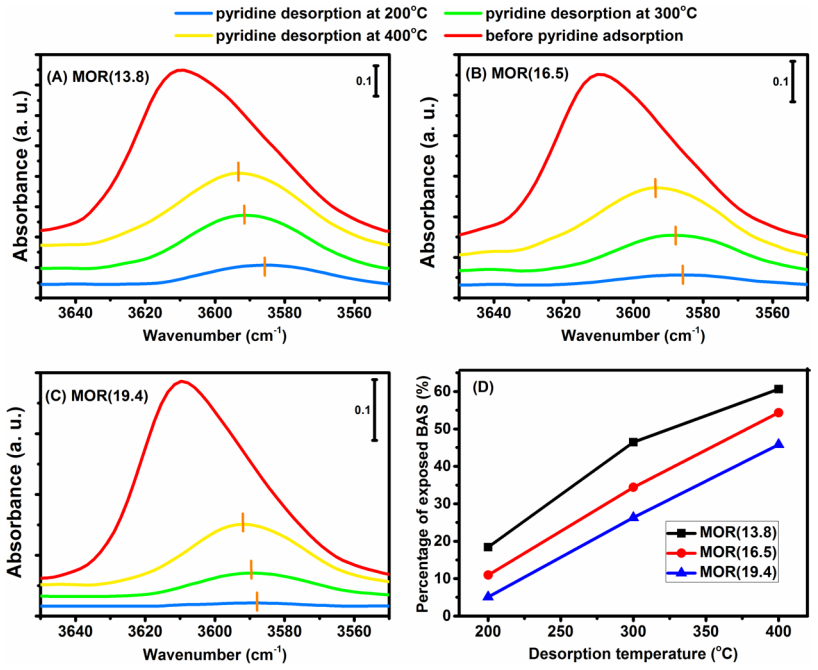

Figure 3. ν(OH) bands of the H-MOR samples after pyridine desorption at different temperatures (A−C) and the recovery percentage of BAS at different desorption temperatures (D). The calculations in (D) are based on the variation of the band areas at 1540 cm^{-1} (Figure S9), because the absorption coefficients of the acidic ν(OH) bands (3650−3550 cm^{-1}) may vary with the locations of acidic hydroxyls.[13,17,58]

existence of defect sites in the samples (Figures 1 and S6), which enlarges the window size of the pockets.

For low-Si samples H-MOR(7.0) and H-MOR(9.7), only a small amount of acid sites could be titrated by pyridine at room temperature. Such distinct pyridine adsorption behaviors, as compared to those of high-Si MOR samples, should be owing to their higher acid density, which causes higher local pyridine density and thus larger diffusion resistance. In addition, the relatively high EFAl content in H-MOR(7.0) and H-MOR(9.7) may also aggravate the difficulty in pyridine diffusion. With an increase in the adsorption temperature to 100 °C, the accessibility of BAS is improved due to the enhanced diffusion, but no preferential location is observed for pyridine molecules.

Pyridine Desorption. The temperature-dependent desorption of pyridine is monitored by FTIR (Figures 3 and S9). The desorption behaviors are observed to be qualitatively similar for high-Si samples MOR(13.8), MOR(16.5), and MOR(19.4), showing gradual recovery of acidic hydroxyls with the temperature ramp until 400 °C. As seen from Figure 3, although the recovery degree at the same temperature differs among the three samples, it is clear that a large proportion of BAS is not restored even after desorption at 400 °C, in agreement with the high acid strength of the BAS as revealed by the NH_3-TPD results. More interestingly, pyridine is observed to escape merely from 8-MR side pockets, as evidenced by the gradual growth of the symmetrical band centered below 3592 cm^{-1}. This phenomenon seems to contradict to the higher acid strength of the BAS in the 8-MR pockets as revealed previously.[20,54] The logic is speculated to be related to the existence of a certain steric effect between pyridine and 8-MR pockets. It is acknowledged that a strong coulombic field exists in the negative framework of zeolites, and it could disturb the electron clouds of the accommodated guest molecules.[55] This disturbance is especially prominent when the size of guest molecules matches well with the zeolite cages. Under such circumstances, a contraction of the molecular orbitals of guest molecules would occur due to a strong electronic confinement effect.[56,57] Therefore, the enhanced lattice vibration of 8-MR windows at a higher temperature, together with the assistance of the delocalized electron cloud in 8-MR pockets, might help breathe out the adsorbed pyridine in their proximity, leading to the preferential recovery of 8-MR hydroxyls. The high recovery proportion in MOR(13.8) shown in Figure 3D possibly relates to its relatively intact framework, which exerts a stronger confinement effect on pyridine adspecies in 8-MR pockets and thus reduces their adsorption stability.

Another interesting phenomenon is that the absorption bands due to the exposed hydroxyls show a gradual shift toward higher frequencies (from 3585 to 3592 cm^{-1}) with the increase of desorption temperature, implying the heterogeneity of the BAS on MOR zeolite. Lukyanov et al. once carried out FTIR investigation on the BAS in MOR zeolite. Using the Fourier self-deconvolution method,[13] they identified the existence of six different Brønsted hydroxyl bands arising from different crystallographic positions, among which three HF bands at 3625, 3617, and 3609 cm^{-1} are located in the 12-MR channels, two LF bands at 3591 and 3581 cm^{-1} are located in the 8-MR pockets, and one band at 3599 cm^{-1} is at the intersections between the pockets and 12-MR channels. These results are in good congruence with our findings.

For pyridine-modified low-Si samples MOR(7.0) and MOR(9.7), although their acid sites cannot be completely covered after pyridine adsorption at 100 °C, they show similar desorption behaviors to high-Si samples with the preferential recovery of acid sites in 8-MR pockets upon heating (Figure S10). In addition, sample MOR(7.0) shows a more obvious HF shift of the bridging hydroxyl band, following an increase of the desorption temperature. Its hydroxyl peak moves to 3601 cm^{-1} after desorption at 400 °C, implying increased pyridine desorption from the 12-MR channels. This phenom-

https://dx.doi.org/10.1021/acscatal.9b04890
ACS Catal. 2020, 10, 3372−3380

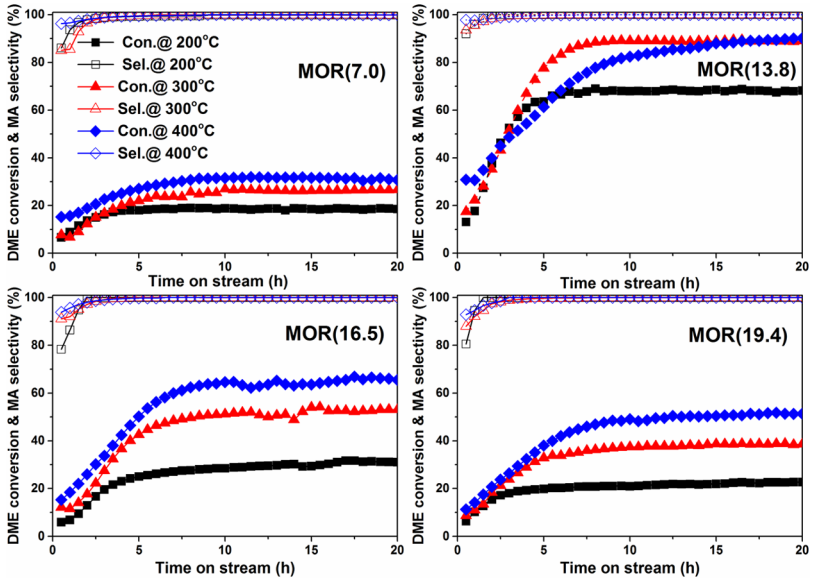

Figure 4. DME conversion and MA selectivity over pyridine-modified H-MOR catalysts after pretreatment at different pyridine desorption temperatures. Reaction conditions: 200 °C, 2 MPa, DME/CO/N_2 = 5/35/60, GHSV = 3600 mL/g/h.

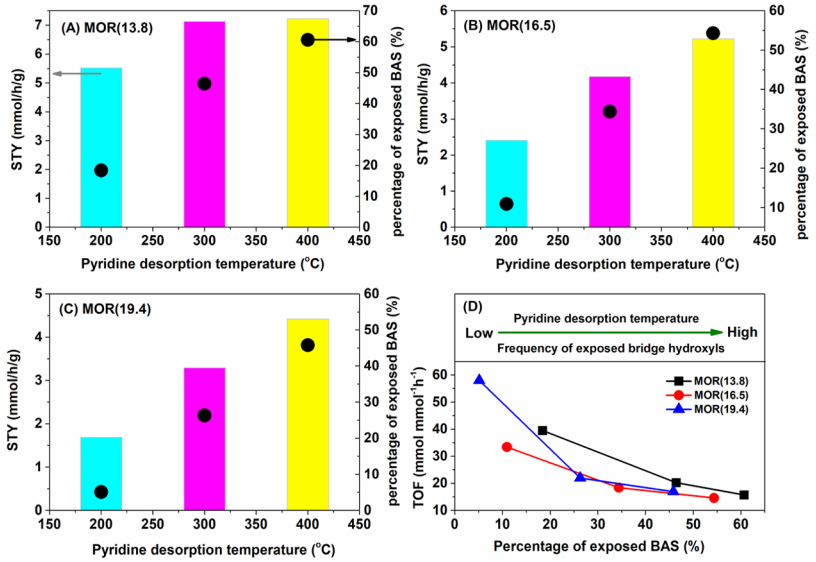

Figure 5. MA space-time yield (bar chart, TOS = 20 h) and the percentage of exposed BAS (black circles) at different pyridine desorption temperatures on the H-MOR zeolites (A−C). (D) presents the variation of the TOF of the catalysts following BAS exposure. The percentage of exposed BAS is from Figure 3D. The exposed BAS amount for TOF calculation is evaluated based on the total BAS in Table 2 and its exposed percentage. They are mainly from the 8-MR pockets when desorption temperature is less than 400 °C.

enon might be due to the interference between the adjacent protonated pyridine in 12-MR channels with high acid density.

Catalytic Performance for DME Carbonylation. The DME carbonylation performances of the pyridine-modified H-MOR zeolites were evaluated under different pyridine desorption conditions, and the corresponding DME conversion and MA selectivity versus time on stream (TOS) are illustrated in Figure 4. All of the investigated catalysts exhibit an induction period with lower DME conversion at the beginning of the reaction, which should be due to the interaction of DME with the BAS and the formation of surface methoxyl species.[14] As the reaction proceeds, the conversion rises rapidly and reaches a steady plateau. A similar variation trend could be observed for MA selectivity, giving a steady value of around 100%. Moreover, the steady DME conversions increase in parallel with pyridine desorption temperatures (200−400 °C) for all of the samples. The rationale lies in the fact that pyridine actually enters the 8-MR pockets during its pre-adsorption procedure; the carbonylation activity centers inside the pockets are gradually exposed, following an increase of the desorption temperature. It is noted that further increasing the desorption temperature to 500 °C would lead to decreased carbonylation activity and stability (Figure S11). An obvious deactivation trend can be observed within 20 h. This should be caused by the exposure of the acid sites in 12-MR channels[15,20,29] and the carbonization of part of pyridine at high temperature.[10] These results imply that pyridine desorption temperatures essentially determine the carbonylation activity and stability of the pyridine-modified MOR catalysts.

https://dx.doi.org/10.1021/acscatal.9b04890
ACS Catal. 2020, 10, 3372−3380

The DME conversion activity follows a volcanic trend as a function of the Si/Al ratios. MOR(13.8) exhibits the best DME carbonylation activity, independent of the pyridine desorption temperatures. The reason behind this should be multifold. First, MOR(13.8) possesses relatively strong acidity, as revealed by NH_3-TPD analysis. Besides, for sample MOR(7.0) with a lower Si/Al ratio, the excessive acid density causes an overcrowdedness of pyridine molecules within the 12-MR channels (see the Pyridine Adsorption and Pyridine Desorption sections) and consequently exerts a negative effect on the diffusion of reactants and products. For high-Si samples MOR(13.8), MOR(16.5), and MOR(19.4), the relatively low acid densities are beneficial to the improvement of mass transfer. Compared to MOR(13.8), the inferior catalytic performances of MOR(16.5) and MOR(19.4) should result from their fewer active sites. As a consequence, sample MOR(13.8) with higher acid strength and optimal acid density exhibits the best DME carbonylation performance. In addition, the existence of defects such as silanol nests or aluminols is less obvious for sample MOR(13.8). The negative effect of these defects on DME carbonylation could not be excluded and deserves further study.

Figure 5 presents the space-time yield (STY) of MA and the percentage of exposed BAS at different desorption temperatures over high-Si H-MOR catalysts. It can be seen that the STY of MA from MOR(13.8) reaches as high as 7.2 mmol/(h g) when the pyridine desorption temperatures are higher than 300 °C. This value is the highest ever reported for the MOR-catalyzed DME carbonylation reaction (Table S2). However, it is noted that the increase of STY is not linearly proportional to the increased BAS exposure, despite the fact that the majority of these BAS are from the 8-MR pockets (see Figure 3). The turnover frequency (TOF) of the samples at different desorption temperatures is further calculated and plotted against the percentage of the exposed BAS. As shown in Figure 5D, the TOF value drops significantly following the exposure of BAS for all of the samples, which reveals that the catalytic activity of the BAS inside the 8-MR pockets is inhomogeneous; the BAS exposed at lower desorption temperatures possess superior catalytic activity. As the above Py-FTIR results have demonstrated that the LF acidic hydroxyls of the 8-MR pockets are preferentially exposed upon pyridine desorption, it is concluded that these sites with LF vibrations have the highest carbonylation activity.

To explore the location of the LF hydroxyls in the pockets, we tried to prepare pyridine-exchanged MOR(13.8) by ion-exchanging the calcined Na-form sample with pyridine aqueous solution and found that the Na/Al ratio of the sample decreased from 0.76 to 0.13 after the ion exchange. Previous work reported that there are three positions for Na^+ cations in the structure of MOR;[59] the ratio of Na^+ in unconstrained and constrained environments is 1:2.[28] Herein, such a low Na content implies the incorporation of pyridine into the pockets. We suppose that the residual Na^+ cations are located at the bottom of the pockets, where the constrained environment limits the exchange with bulky hydrated pyridine ions. As shown in Figure S12, extremely low activity is observed for the pyridine-exchanged MOR(13.8). This suggests that the BAS at the bottom of the 8-MR pockets should be the most active sites for DME carbonylation, which correspond to the LF acidic hydroxyls in the FTIR spectra.

CONCLUSIONS

The adsorption/desorption behaviors of pyridine toward a series of MOR zeolites and their impact on DME carbonylation have been investigated to elucidate the pyridine modification−catalytic property relationships and to improve the catalyst performance. It is demonstrated that pyridine molecules could penetrate into 8-MR pockets and interact with the Brønsted hydroxyls therein. This is likely owing to the existence of defect sites in the MOR framework, which enlarges the window size of the pockets. The Si/Al ratios of MOR zeolites influence the pyridine adsorption process. Low Si/Al ratios, corresponding to the high acid density and relatively large amount of EFAL species, would cause increased diffusion limitation and incomplete acidity coverage. However, for MOR with a higher Si/Al ratio (>10), all of the acid sites can be easily reached by pyridine molecules. With the ramp of the pyridine desorption temperature (≤400 °C), the BAS in 8-MR side pockets are preferentially recovered, leading to incremental conversion. The pyridine desorption temperature essentially determines the carbonylation activity and stability of the catalysts. The DME carbonylation activity follows a volcanic trend with the increase of Si/Al ratios. The optimal Si/Al ratio is around 13.8, over which a high MA yield of 7.2 mmol/(g h) can be achieved under a controlled pyridine desorption temperature (300−400 °C). The higher acid density, stronger acidity, and better diffusion properties corporately contribute to the excellent catalytic performance. The catalytic activity of the BAS in the 8-MR pockets is rather inhomogeneous, and the LF bridging hydroxyls present at the bottom of the side pockets have superior carbonylation activities.

ASSOCIATED CONTENT

Supporting Information

The Supporting Information is available free of charge at https://pubs.acs.org/doi/10.1021/acscatal.9b04890.

Initial gel compositions, the ν(OH) bands of H-MOR pretreated with different heating rates, XRD, SEM, N_2 physisorption isotherms, NH_3-TPD, ^{1}H MAS NMR spectra, the deconvoluted ν(OH) bands of FTIR spectra, the derivation of the isolated Brønsted ν(OH) band for deconvolution, the FTIR spectra of pyridine ring-related vibration regions, the ν(OH) bands of the low-Si H-MOR samples after pyridine desorption at different temperatures, the DME carbonylation activities of the samples after pyridine desorption at 500 °C, the detailed procedure for pyridine exchange and the DME carbonylation activities of the pyridine-exchanged sample, the summary of the product STY in the zeolite-catalyzed DME carbonylation reaction (PDF)

AUTHOR INFORMATION

Corresponding Authors

Peng Tian − *National Engineering Laboratory for Methanol to Olefins, Dalian National Laboratory for Clean Energy, Dalian Institute of Chemical Physics, Chinese Academy of Sciences, Dalian 116023, China*; Email: tianpeng@dicp.ac.cn

Zhongmin Liu − *National Engineering Laboratory for Methanol to Olefins, Dalian National Laboratory for Clean Energy, Dalian Institute of Chemical Physics, Chinese Academy of Sciences, Dalian 116023, China*; orcid.org/0000-0002-7999-2940; Email: liuzm@dicp.ac.cn

https://dx.doi.org/10.1021/acscatal.9b04890
ACS Catal. 2020, 10, 3372−3380

Authors

Kaipeng Cao − *National Engineering Laboratory for Methanol to Olefins, Dalian National Laboratory for Clean Energy, Dalian Institute of Chemical Physics, Chinese Academy of Sciences, Dalian 116023, China; University of Chinese Academy of Sciences, Chinese Academy of Sciences, Beijing 100049, China*

Dong Fan − *National Engineering Laboratory for Methanol to Olefins, Dalian National Laboratory for Clean Energy, Dalian Institute of Chemical Physics, Chinese Academy of Sciences, Dalian 116023, China*

Lingyun Li − *National Engineering Laboratory for Methanol to Olefins, Dalian National Laboratory for Clean Energy, Dalian Institute of Chemical Physics, Chinese Academy of Sciences, Dalian 116023, China*

Benhan Fan − *National Engineering Laboratory for Methanol to Olefins, Dalian National Laboratory for Clean Energy, Dalian Institute of Chemical Physics, Chinese Academy of Sciences, Dalian 116023, China; University of Chinese Academy of Sciences, Chinese Academy of Sciences, Beijing 100049, China*

Linying Wang − *National Engineering Laboratory for Methanol to Olefins, Dalian National Laboratory for Clean Energy, Dalian Institute of Chemical Physics, Chinese Academy of Sciences, Dalian 116023, China*

Dali Zhu − *National Engineering Laboratory for Methanol to Olefins, Dalian National Laboratory for Clean Energy, Dalian Institute of Chemical Physics, Chinese Academy of Sciences, Dalian 116023, China; University of Chinese Academy of Sciences, Chinese Academy of Sciences, Beijing 100049, China*

Quanyi Wang − *National Engineering Laboratory for Methanol to Olefins, Dalian National Laboratory for Clean Energy, Dalian Institute of Chemical Physics, Chinese Academy of Sciences, Dalian 116023, China*

Complete contact information is available at: https://pubs.acs.org/10.1021/acscatal.9b04890

Author Contributions

[§]K.C. and D.F. contributed equally to this work.

Notes

The authors declare no competing financial interest.

■ ACKNOWLEDGMENTS

The authors acknowledge the National Natural Science Foundation of China (Nos. 91545104, 21606221, 21676262 and 21991091) and the Key Research Program of Frontier Sciences, Chinese Academy of Sciences (Grant No. QYZDB-SSW-JSC040).

■ REFERENCES

(1) Cheung, P.; Bhan, A.; Sunley, G. J.; Iglesia, E. Selective carbonylation of dimethyl ether to methyl acetate catalyzed by acidic zeolites. *Angew. Chem., Int. Ed.* **2006**, *45*, 1617−1620.

(2) Rasmussen, D. B.; Christensen, J. M.; Temel, B.; Studt, F.; Moses, P. G.; Rossmeisl, J.; Riisager, A.; Jensen, A. D. Ketene as a Reaction Intermediate in the Carbonylation of Dimethyl Ether to Methyl Acetate over Mordenite. *Angew. Chem., Int. Ed.* **2015**, *54*, 7261−7264.

(3) Reule, A. A. C.; Semagina, N. Zinc Hinders Deactivation of Copper-Mordenite: Dimethyl Ether Carbonylation. *ACS Catal.* **2016**, *6*, 4972−4975.

(4) Goldemberg, J. Ethanol for a sustainable energy future. *Science* **2007**, *315*, 808−810.

(5) Grad, P. Debut of a Coal-to-Ethanol Plant. https://www.chemengonline.com/debut-coal-ethanol-plant/.

(6) Liu, Y.; Zhao, N.; Xian, H.; Cheng, Q.; Tan, Y.; Tsubaki, N.; Li, X. Facilely Synthesized H-Mordenite Nanosheet Assembly for Carbonylation of Dimethyl Ether. *ACS Appl. Mater. Interfaces* **2015**, *7*, 8398−8403.

(7) Li, Y.; Sun, Q.; Huang, S. Y.; Cheng, Z. Z.; Cai, K.; Lv, J.; Ma, X. B. Dimethyl ether carbonylation over pyridine-modified MOR: Enhanced stability influenced by acidity. *Catal. Today* **2018**, *311*, 81−88.

(8) Zhang, Z. T.; Zhao, N.; Ma, K.; Cheng, Q. P.; Zhang, J.; Zheng, L. R.; Tian, Y.; Li, X. G. Isolated zinc in mordenite stabilizing carbonylation of dimethyl ether to methyl acetate. *Chin. Chem. Lett.* **2019**, *30*, 513−516.

(9) Zhao, N.; Cheng, Q.; Lyu, S.; Guo, L.; Tian, Y.; Ding, T.; Xu, J.; Ma, X.; Li, X. Promoting dimethyl ether carbonylation over hot-water pretreated H-mordenite. *Catal. Today* **2020**, *339*, 86−92.

(10) Zhao, N.; Tian, Y.; Zhang, L.; Cheng, Q.; Lyu, S.; Ding, T.; Hu, Z.; Ma, X.; Li, X. Spacial hindrance induced recovery of over-poisoned active acid sites in pyridine-modified H-mordenite for dimethyl ether carbonylation. *Chin. J. Catal.* **2019**, *40*, 895−904.

(11) Moliner, M.; Martinez, C.; Corma, A. Multipore Zeolites: Synthesis and Catalytic Applications. *Angew. Chem., Int. Ed.* **2015**, *54*, 3560−3579.

(12) Li, X.; Prins, R.; van Bokhoven, J. A. Synthesis and characterization of mesoporous mordenite. *J. Catal.* **2009**, *262*, 257−265.

(13) Lukyanov, D. B.; Vazhnova, T.; Cherkasov, N.; Casci, J. L.; Birtill, J. J. Insights into Bronsted Acid Sites in the Zeolite Mordenite. *J. Phys. Chem. C* **2014**, *118*, 23918−23929.

(14) Cheung, P.; Bhan, A.; Sunley, G. J.; Law, D. J.; Iglesia, E. Site requirements and elementary steps in dimethyl ether carbonylation catalyzed by acidic zeolites. *J. Catal.* **2007**, *245*, 110−123.

(15) Boronat, M.; Martinez-Sanchez, C.; Law, D.; Corma, A. Enzyme-like Specificity in Zeolites: A Unique Site Position in Mordenite for Selective Carbonylation of Methanol and Dimethyl Ether with CO. *J. Am. Chem. Soc.* **2008**, *130*, 16316−16323.

(16) Li, B.; Xu, J.; Han, B.; Wang, X.; Qi, G.; Zhang, Z.; Wang, C.; Deng, F. Insight into Dimethyl Ether Carbonylation Reaction over Mordenite Zeolite from in-Situ Solid-State NMR Spectroscopy. *J. Phys. Chem. C* **2013**, *117*, 5840−5847.

(17) Bhan, A.; Allian, A. D.; Sunley, G. J.; Law, D. J.; Iglesia, E. Specificity of sites within eight-membered ring zeolite channels for carbonylation of methyls to acetyls. *J. Am. Chem. Soc.* **2007**, *129*, 4919−4924.

(18) Wang, M. X.; Huang, S. Y.; Lu, J.; Cheng, Z. Z.; Li, Y.; Wang, S. P.; Ma, X. B. Modifying the acidity of H-MOR and its catalytic carbonylation of dimethyl ether. *Chin. J. Catal.* **2016**, *37*, 1530−1538.

(19) Bhan, A.; Iglesia, E. A link between reactivity and local structure in acid catalysis on zeolites. *Acc. Chem. Res.* **2008**, *41*, 559−567.

(20) Rasmussen, D. B.; Christensen, J. M.; Temel, B.; Studt, F.; Moses, P. G.; Rossmeisl, J.; Riisager, A.; Jensen, A. D. Reaction mechanism of dimethyl ether carbonylation to methyl acetate over mordenite a combined DFT/experimental study. *Catal. Sci. Technol.* **2017**, *7*, 1141−1152.

(21) Liu, Z. Q.; Yi, X. F.; Wang, G. R.; Tang, X. M.; Li, G. C.; Huang, L.; Zheng, A. M. Roles of 8-ring and 12-ring channels in mordenite for carbonylation reaction: From the perspective of molecular adsorption and diffusion. *J. Catal.* **2019**, *369*, 335−344.

(22) Xue, H. F.; Huang, X. M.; Zhan, E. S.; Ma, M.; Shen, W. J. Selective dealumination of mordenite for enhancing its stability in dimethyl ether carbonylation. *Catal. Commun.* **2013**, *37*, 75−79.

(23) Reule, A. A. C.; Sawada, J. A.; Semagina, N. Effect of selective 4-membered ring dealumination on mordenite-catalyzed dimethyl ether carbonylation. *J. Catal.* **2017**, *349*, 98−109.

(24) Wang, X.; Li, R.; Yu, C.; Liu, Y.; Zhang, L.; Xu, C.; Zhou, H. Enhancing the dimethyl ether carbonylation performance over mordenite catalysts by simple alkaline treatment. *Fuel* **2019**, *239*, 794−803.

(25) Liu, J.; Xue, H.; Huang, X.; Wu, P.-H.; Huang, S.-J.; Liu, S.-B.; Shen, W. Stability Enhancement of H-Mordenite in Dimethyl Ether Carbonylation to Methyl Acetate by Pre-adsorption of Pyridine. *Chin. J. Catal.* **2010**, *31*, 729−738.
(26) Jiao, F.; Pan, X.; Gong, K.; Chen, Y.; Li, G.; Bao, X. Shape-Selective Zeolites Promote Ethylene Formation from Syngas via a Ketene Intermediate. *Angew. Chem., Int. Ed.* **2018**, *57*, 4692−4696.
(27) He, T.; Hou, G. J.; Li, J. J.; Liu, X. C.; Xu, S. T.; Han, X. W.; Bao, X. H. Highly selective methanol-to-olefin reaction on pyridine modified H-mordenite. *J. Energy Chem.* **2017**, *26*, 354−358.
(28) Marie, O.; Massiani, P.; Thibault-Starzyk, F. Infrared evidence of a third bronsted site in mordenites. *J. Phys. Chem. B* **2004**, *108*, 5073−5081.
(29) Datka, J.; Gil, B.; Kubacka, A. Acid properties of NaH-mordenites - infrared spectroscopic studies of ammonia sorption. *Zeolites* **1995**, *15*, 501−506.
(30) Hayashi, S.; Kojima, N. Acid properties of H-type mordenite studied by solid-state NMR. *Microporous Mesoporous Mater.* **2011**, *141*, 49−55.
(31) Wang, X. S.; Li, R. J.; Yu, C. C.; Liu, Y. X.; Liu, L. M.; Xu, C. M.; Zhou, H. J.; Lu, C. X. Influence of Acid Site Distribution on Dimethyl Ether Carbonylation over Mordenite. *Ind. Eng. Chem. Res.* **2019**, *58*, 18065−18072.
(32) Sasaki, H.; Oumi, Y.; Itabashi, K.; Lu, B. W.; Teranishi, T.; Sano, T. Direct hydrothermal synthesis and stabilization of high-silica mordenite (Si:Al = 25) using tetraethylammonium and fluoride ions. *J. Mater. Chem.* **2003**, *13*, 1173−1179.
(33) Conato, M. T.; Oleksiak, M. D.; McGrail, B. P.; Motkuri, R. K.; Rimer, J. D. Framework stabilization of Si-rich LTA zeolite prepared in organic-free media. *Chem. Commun.* **2015**, *51*, 269−272.
(34) Schroeder, C.; Hansen, M. R.; Koller, H. Ultrastabilization of Zeolite Y Transforms Bronsted-Bronsted Acid Pairs into Bronsted-Lewis Acid Pairs. *Angew. Chem., Int. Ed.* **2018**, *57*, 14281−14285.
(35) Bagnasco, G. Improving the selectivity of NH3 TPD measurements. *J. Catal.* **1996**, *159*, 249−252.
(36) Lónyi, F.; Valyon, J. On the interpretation of the NH3-TPD patterns of H-ZSM-5 and H-mordenite. *Microporous Mesoporous Mater.* **2001**, *47*, 293−301.
(37) Wang, H. L.; Xin, W. Y. Surface acidity of H-beta and its catalytic activity for alkylation of benzene with propylene. *Catal. Lett.* **2001**, *76*, 225−229.
(38) Rodríguez-González, L.; Hermes, F.; Bertmer, M.; Rodriguez-Castellon, E.; Jimenez-Lopez, A.; Simon, U. The acid properties of H-ZSM-5 as studied by NH_3-TPD and Al-27-MAS-NMR spectroscopy. *Appl. Catal., A* **2007**, *328*, 174−182.
(39) Benaliouche, F.; Boucheffa, Y.; Ayrault, P.; Mignard, S.; Magnoux, P. NH3-TPD and FTIR spectroscopy of pyridine adsorption studies for characterization of Ag- and Cu-exchanged X zeolites. *Microporous Mesoporous Mater.* **2008**, *111*, 80−88.
(40) Zhou, D. H.; He, N.; Wang, Y. Q.; Yang, G.; Liu, X. C.; Bao, X. H. DFT study of the acid strength of MCM-22 with double Si/Al substitutions in 12MR supercage. *J. Mol. Struct.: THEOCHEM* **2005**, *756*, 39−46.
(41) Niwa, M.; Katada, N.; Sawa, M.; Murakami, Y. Temperature-programmed desorption of ammonia with readsorption based on the derived theoretical equation. *J. Phys. Chem. A* **1995**, *99*, 8812−8816.
(42) Park, J. W.; Kim, S. J.; Seo, M.; Kim, S. Y.; Sugi, Y.; Seo, G. Product selectivity and catalytic deactivation of MOR zeolites with different acid site densities in methanol-to-olefin (MTO) reactions. *Appl. Catal., A* **2008**, *349*, 76−85.
(43) Zhang, J.; Xu, L.; Zhang, Y.; Huang, Z.; Zhang, X.; Zhang, X.; Yuan, Y.; Xu, L. Hydrogen transfer versus olefins methylation: On the formation trend of propene in the methanol-to-hydrocarbons reaction over Beta zeolites. *J. Catal.* **2018**, *368*, 248−260.
(44) Emeis, C. A. Determination of integrated molar extinction coefficients for infrared-absorption bands of pyridine adsorbed on solid acid catalysts. *J. Catal.* **1993**, *141*, 347−354.
(45) Maache, M.; Janin, A.; Lavalley, J. C.; Benazzi, E. FT infrared study of bronsted acidity of H-mordenites - heterogeneity and effect of dealumination. *Zeolites* **1995**, *15*, 507−516.
(46) Pastvova, J.; Pilar, R.; Moravkova, J.; Kaucky, D.; Rathousky, J.; Sklenak, S.; Sazama, P. Tailoring the structure and acid site accessibility of mordenite zeolite for hydroisomerisation of n-hexane. *Appl. Catal., A* **2018**, *562*, 159−172.
(47) Nesterenko, N. S.; Thibault-Starzyk, F.; Montouillout, V.; Yuschenko, V. V.; Fernandez, C.; Gilson, J. P.; Fajula, F.; Ivanova, I. I. Accessibility of the acid sites in dealuminated small-port mordenites studied by FTIR of co-adsorbed alkylpyridines and CO. *Microporous Mesoporous Mater.* **2004**, *71*, 157−166.
(48) Dessau, R. M.; Schmitt, K. D.; Kerr, G. T.; Woolery, G. L.; Alemany, L. B. On the presence of internal silanol groups in ZSM-5 and the annealing of these sites by steaming. *J. Catal.* **1987**, *104*, 484−489.
(49) Krijnen, S.; Harmsen, R. J.; Abbenhuis, H. C. L.; Van Hooff, J. H. C.; Van Santen, R. A. Incompletely condensed silasesquioxanes as models for zeolite defect sites: an FTIR and density functional study. *Chem. Commun.* **1999**, 501−502.
(50) Wu, P.; Komatsu, T.; Yashima, T. Ir and Mas Nmr-Studies on the Incorporation of Aluminum Atoms into Defect Sites of Dealuminated Mordenites. *J. Phys. Chem. B* **1995**, *99*, 10923−10931.
(51) Zholobenko, V. L.; Makarova, M. A.; Dwyer, J. Inhomogeneity of Bronsted acid sites in H-mordenite. *J. Phys. Chem. C* **1993**, *97*, 5962−5964.
(52) Wakabayashi, F.; Kondo, J.; Wada, A.; Domen, K.; Hirose, C. FT-IR studies of the interaction between zeolitic hydroxyl-groups and small molecules. 1. Adsorption of nitrogen on H-mordenite at low-temperature. *J. Phys. Chem. D* **1993**, *97*, 10761−10768.
(53) Li, L. Y.; Wang, Q. Y.; Liu, H. C.; Sun, T. T.; Fan, D.; Yang, M.; Tian, P.; Liu, Z. M. Preparation of Spherical Mordenite Zeolite Assemblies with Excellent Catalytic Performance for Dimethyl Ether Carbonylation. *ACS Appl. Mater. Interfaces* **2018**, *10*, 32239−32246.
(54) Niwa, M.; Suzuki, K.; Katada, N.; Kanougi, T.; Atoguchi, T. Ammonia IRMS-TPD study on the distribution of acid sites in mordenite. *J. Phys. Chem. B* **2005**, *109*, 18749−18757.
(55) Barthomeuf, D. Zeolites as Adsorbents and Catalysts. The Interactive System Encaged Molecule/Zeolite Framework. In *Progress in Zeolite and Microporous Materials*; Chon, H.; Ihm, S. K.; Uh, Y. S., Eds.; Elsevier Science BV: Amsterdam, 1997; Vol. *105*, pp 1677−1706.
(56) Gackowski, M.; Podobinski, J.; Hunger, M. Evidence for a strong polarization of n-hexane in zeolite H-ZSM-5 by FT-IR and solid-state NMR spectroscopy. *Microporous Mesoporous Mater.* **2019**, *273*, 67−72.
(57) Zicovich-Wilson, C. M.; Corma, A.; Viruela, P. Electronic Confinement of Molecules in Microscopic Pores. A New Concept Which Contributes to the Explanation of the Catalytic Activity of Zeolites. *J. Phys. Chem. E* **1994**, *98*, 10863−10870.
(58) Makarova, M. A.; Wilson, A. E.; vanLiemt, B. J.; Mesters, C.; deWinter, A. W.; Williams, C. Quantification of Bronsted acidity in mordenites. *J. Catal* **1997**, *172*, 170−177.
(59) Devautour, S.; Henn, F.; Giuntini, J. C.; Zanchetta, J. V.; Vanderschueren, J. TSDC relaxation map analysis in a Na-mordenite zeolite. *Solid State Ionics* **1999**, *122*, 105−111.

https://dx.doi.org/10.1021/acscatal.9b04890
ACS Catal. 2020, 10, 3372−3380